scientific reports

OPEN

Defect states in magnetically "seasoned" WSSe – adsorption and doping effects of magnetic transition metals X = V, Cr, Mn, Fe, Co – a comprehensive first-principles study

Yisehak Gebredingle[1]✉, Heesang Kim[1,2] & Nammee Kim[1]✉

Besides the symmetry breaking of Janus transition metal dichalcogenides (TMDs), Janus-based Diluted Magnetic Semiconductors (DMS) are attractive to study considering the local symmetry of transition metal (TM) dopant/adatom. This study conducts a first-principles calculation of magnetic properties in TM (V, Cr, Mn, Fe, and Co) -- doped and adsorbed Janus WSSe. Our results reveal that TM's atomic/ionic size impacts *d-p-d* orbital overlap, affecting bond length/angle and defect state positions. The result shows that V-doped WSSe exhibits long-range ferromagnetic order sustained by itinerant carriers and W atom spin-orbital coupling (SOC). The mechanism of *d-p-d* orbital hybridization is highlighted with an overlapping density of states and spin-density plots. Moreover, an enhanced magnetic anisotropy energy (MAE) is observed in Fe/Co-doped and Mn/Fe-adsorbed systems, with the easy axis aligning to the *c*-axis. The orbital contribution of MAE provided explains the relationship between states near the Fermi and MAE. On the other hand, the adsorption of V and Cr aligns the easy axis to the *a-b* plane, for which we have systematically explained the contribution of the spin-flip term in MAE. This research provides insights and a guideline for further exploration of 2D DMS for spintronics and spin-related phenomena.

Keywords WSSe, Defect states, Doping, Adsorption, *d-p-d* hybridization, Magnetic anisotropy

Diluted magnetic semiconductors (DMS) have been extensively investigated due to their potential in spintronics applications and for discovering fundamental spin-related phenomena[1–4]. To stabilize the long-range spin order in bulk DMS materials, two main magnetic interaction mechanisms have been proposed: (1) direct interactions between the dopants (through their overlapped wave functions) and (2) indirect interactions through itinerant carriers[5–7]. The former requires a high dopant concentration, while the latter uses spin-polarized itinerant holes at a low dopant concentration[7]. On the other hand, over the last 5-years, **intrinsic two-dimensional (2D) magnetic materials** have received significant attention due to their intrinsic long-range spin order and benefits in atomic-size magnets as promising candidates for miniaturized spintronics devices. Moreover, despite promising progress in different 2D van der Waal magnetic materials like $Cr_2Ge_2Te_6$[8], Fe_xGTe_2(FGT)[9,10], and VSe_2[11], their limitations of working ambient conditions (due to low Curie temperature (T_C) and high surface energy), pose a challenge for the scientific community[12,13]. While recently inaugurated ultra-thin non-van der Waal materials like $Cr_2\times_3$(X = S, Se, and Te) give another glimpse of hope to overcome these difficulties, a lot is to wait for the practical device applications[14–16]. Consequently, the search for atomically thin magnetic materials has stretched to the artificially induced magnetism in 2D transition metal dichalcogenide (TMD) **2D diluted magnetic semiconductors (DMS)**[17–24]. Besides, recent reports show that 2D materials with **heavy atoms like tungsten (W)** are good candidates for which long-range magnetic ordering is kept pronounced by the relativistic electron-atom effect—spin-orbit coupling (SOC) on W atom *d*states[25–27].

[1]Department of Physics, Soongsil University, Seoul 06978, South Korea. [2]OMEG Institute, Soongsil University, Seoul 06978, South Korea. ✉email: yisehakgd@ssu.ac.kr; nammee@ssu.ac.kr

Recent experimental discoveries of **Janus**versions of TMD (MXY, X≠Y; M = TM, X/Y = S, Se, and Te) have shown that they possess out-of-plane piezoelectric polarization and strong Rashba effect due to their unequal potential on the two faces[28–34]. Accordingly, the **most studied possible applications**are photo-catalytic water splitting, a catalyst for the hydrogen evolution reaction (HER), gas sensing devices, optoelectronics, and electromechanical devices[35–42]. Additionally, artificially induced magnetism in WSSe (i.e., doping, adsorption, and proximity effect) has been reported to show valley polarization[43,44]. Recently, X.W. Zhao et al. have demonstrated that big valley polarization up to 58meV and 62meV can be obtained for V doping or Cr adsorption on the Se-surface of WSSe, respectively[43]. Moreover, X. C. She et al. have predicted that varying stacking configurations of WSSe-CrI_3heterostructure valley polarization can be tuned[44]. Kai Chen et al. showed the adsorption effect of transition metal (TM) atoms V, Cr, Mn, Fe, and Co on both surfaces of WSSe, showing the possible magnetization of WSSe via charge transfer[45]. Besides, they have observed that the induced magnetism for TM adsorbed onto the S surface of WSSe is stronger than Se-Surface-adsorption due to electrostatic potential and the easy axis for Fe adatom switches from in-plane (on-S surface) to off-plane (on-Se surface). Although some efforts have been made in the computational study of TM-doped/adsorbed magnetic WSSe[43,45–48], **a comprehensive and systematic approach** is still lacking.

In this work, we conducted first-principles calculations to elucidate the magnetic properties of TMs (V, Cr, Mn, Fe, Co) both doped and adsorbed WSSe. The careful observation of the **relationship** between rearranged structure, *d-p-d* hybridization, and magnetic anisotropy energy (MAE) shows that the atomic/ionic size of TM has a crucial impact on the *d-d* orbital overlap and, therefore, on bond length/angle and position of defect states. **Long-range ferromagnetic**(FM) order is shown in the V-doped WSSe system, which is maintained by the SOC of the W atom, which is in line with the previous reports of other TMD[25–27]. **A local symmetry breaking** observed in Fe/Co-doped and Mn/Fe-adsorbed on the S-surface of WSSe causes an enhanced MAE. Moreover, the magnetic anisotropy calculation for both TM doped and adsorbed WSSe revealed the *c-axis* as the easy axis and reasoned out the origin of the in-plane easy axis observed in the V/Cr adsorbed system and its **relation with the spin-density distribution**.

The paper is divided into three sections below arranged as: (I) Formation/Binding energies structural parameters, and magnetic moment; (II) Electronic states and spatial distribution of spin-density; and (III) Magnetic anisotropy Energy. The summarized presentation done in this work will serve as a guide for the scientific community's further exploration of 2D DMS.

Computational details

All the spin-polarized first-principle calculations were performed by the commercially available Vienna Ab initio Simulation Package (VASP)[49]. The generalized gradient approximation (GGA) parametrized by Perdew-Burke-Ernzerhof (PBE) is employed to describe the exchange-correlation function[50,51]. For the 3*d*transition metal (TM) elements, adding Hubbard U[51] could improve the description of the localized electronic orbitals. However, it is not straightforward to apply the Hubbard *U* in defect formation energy calculations, which require using identical *U*values when calculating the total energy of the defect supercell and the chemical potential of the TM dopant[52]. Also, the same TM element in different valence states, such as a dopant and adatom, may require different *U*values[53]. Given this uncertainty, we did not include the Hubbard *U*correction in this work. The PBE version of the projector augmented-wave (PAW) was employed to treat valence electrons with plane-wave basis set cutoff energy of 500 eV. We build the model of the 4 × 4 × 1 pristine single-layer WSSe (48 atoms); the vacuum layer is set to 20 Å to avoid the effects generated by the periodic boundary conditions. The Brillouin zone is sampled by a Monkhorst mesh of 3 × 3 × 1 k-points[54]. The formation energy (E_{form}) is calculated as $E_{form}= E_{WSSe(Dopped)}- E_{WSSe(Pure)}- (\mu_{TM}- \mu_{W})$. To determine the adsorption strength between the TM-WSSe monolayer, we used $E_{ads} = E_{WSSe(ads)}- E_{WSSe(Pure)}- (\mu_{TM})$, where $E_{WSSe(Dopped)}$ and $E_{WSSe(Pure)}$ are the total energies of dopped and pure WSSe monolayer, respectively. μ_{TM} is the chemical potential of the transition metal atom taken from energy per atom of the body-centered cubic (bcc) structure, and $\mu_{W}$is the chemical potential of the W atom[52]. Spin density is defined as the difference between the spin-down and spin-up charge densities ($\rho_{\downarrow}$-$\rho_{\uparrow}$). Magnetic anisotropy energy (MAE) is defined as the difference between energies corresponding to the magnetization in the in-plane and out-of-plane directions ($E_{MAE} = E_{\perp} - E_{\parallel}$). Therefore, a positive (negative) value of MAE indicates an in-plane (out-of-plane) easy axis. After self-consistent ground states were achieved, noncollinear and non-self-consistent calculations were performed to evaluate the total energies. In all MAE calculations, spin-orbit interaction was taken into consideration.

Result and discussion

Formation/Binding energies, structural parameters, and magnetic moments

Schematic representations of stable supercell structures of the dopped and adsorbed systems are shown in Fig. 1. The pristine Janus WSSe has bond lengths of 2.42 Å and 2.53 Å for W-S ($\boldsymbol{l_a}$) and W-Se ($\boldsymbol{l_b}$), respectively, in line with the literature[35,37,43,55]. The planar average electrostatic potential shows the broken symmetry of two faces. To induce magnetism in pristine WSSe, we considered both substitutional doping of the W atom and surface adsorption of magnetic transition metal (TM) elements of V, Cr, Mn, Fe, and Co. Substitutional doping of the W atom causes chalcogenide (S and Se) atoms to get closer/away to/from the TM atom, forming different bond lengths, l_a and l_b, Fig. 1(a). For the adsorption system, referring to previous works, a catalytically active face (i.e., S-Side) with the most stable adsorption site (where the adatom is right on the top of the W atoms) is investigated (Fig. 1(b))[40,43,45,46,56].

The dopped and adsorbed system's calculated formation and binding energies and structural and magnetic parameters are listed in Tables 1 and 2. An increasing formation energy (E_f) is shown from V to Co dopant elements. A seamless substitution is predicted for the V dopant (~ 0.008 eV), while a small energy ~ 0.5 eV for the

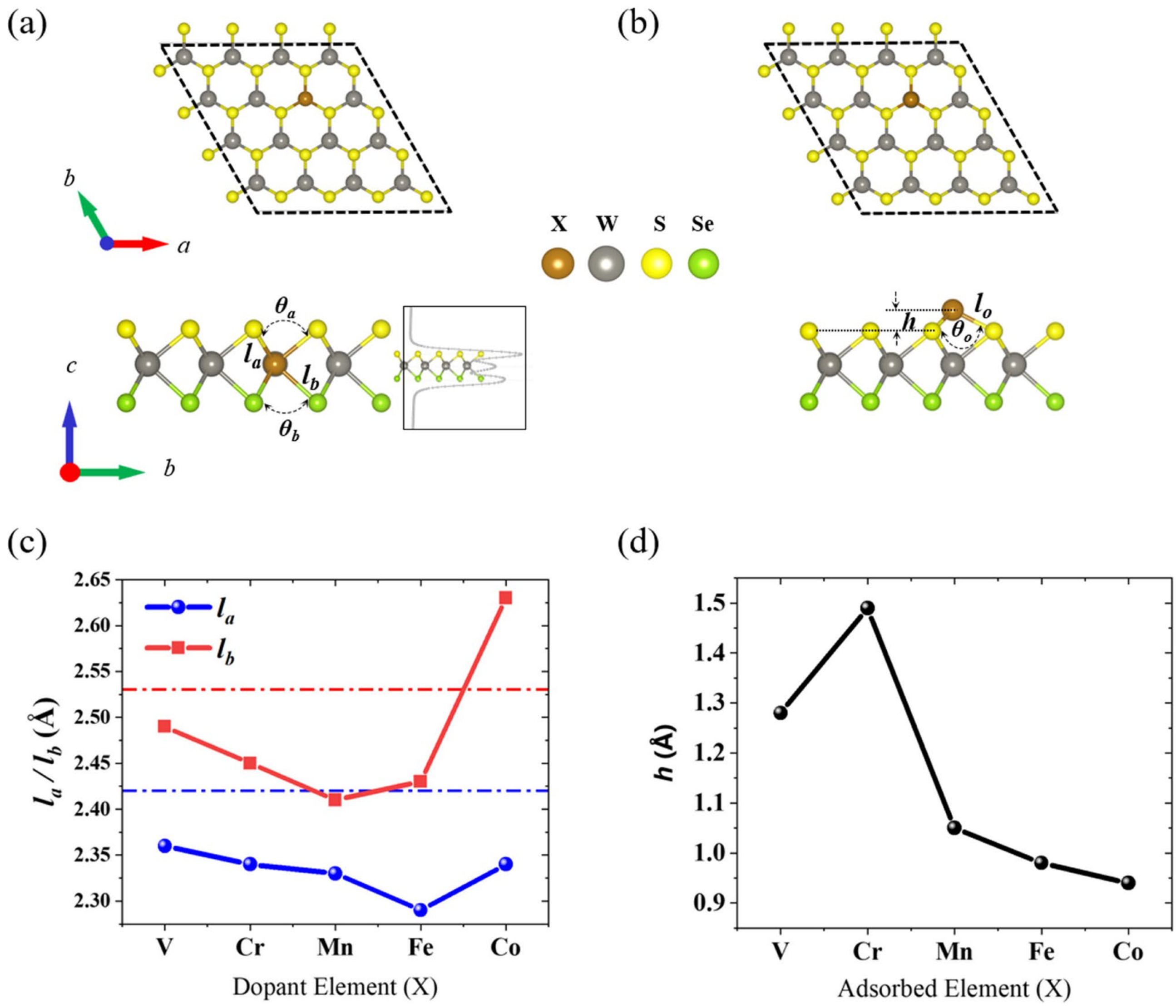

Figure. 1. (Color Online) Schematic representation of relaxed structures of 4 × 4 supercell systems applied and structural parameters. Top and side view of TM doped WSSe (a), and TM adsorbed WSSe (b). Structural parameters, angles; $\boldsymbol{\theta_a}$, $\boldsymbol{\theta_b}$, $\boldsymbol{\theta_o}$, and bond lengths; $\mathbf{l_a}$, $\mathbf{l_b}$, $\mathbf{l_o}$, and adsorption height h_o are marked for each case, and the values are presented in Tables 1 and 2. (c) Bond lengths; X-S ($\mathbf{l_a}$) and X-Se($\mathbf{l_b}$) for each dopant atom in a doped X-WSSe system. Horizontal dashed lines show the pristine WSSe $\mathbf{l_a}$ and $\mathbf{l_b}$ values and solid lines are used to guide the eyes. Average values are taken for local symmetry-breaking bonds in Fe and Co dopant atoms (d) Adsorption height (**h**) for each adatom is measured as the vertical distance from the unperturbed S atoms. The inset at (a) bottom shows the electrostatic potential of pristine WSSe along the c-axis.

Cr dopant indicates a feasible endothermic reaction process[57]. For Mn, Fe, and Co cases, slightly higher energies are required, comparable with reported results on other TMD materials like MoS_2[17]. However, increasing binding energy for Cr, Mn, Fe, and Co is observed for the adsorbed system (Table 2), indicating a relatively easier adsorption process for Mn, Fe, and Co dopants. For V-adsorbed WSSe, however, the adsorption energy comes (-2.2 eV) comparable with that of Fe (-1.98 eV) and Co (-2.62 eV). Besides, the adsorption energies for all TM atom cases show lower than – 0.5 eV, which implies a possibility of chemisorption[58,59]. It is worth noting that the nearly zero formation energy shown in the V-dopant calculation result shows a deficiency in the GGA approximation in the PBE framework. With the DFT + U framework, the dependence of formation energy on empirical values representing localized *3d* states for V-doped WSSe is shown in Fig. S1.

Regarding the structural parameters in the dopped system, despite the lower electronegativity of the TM atom (V (3.20), Cr (3.27), Mn (3.34), Fe (3.42), Co (3.49), eV) than that of W (6.78 eV)[60], for all cases, except Co-Se bond, the TM-S/Se bond length is shorter than that of the W-S/Se bond length (Fig. 1(c)). This can be attributed to the smaller atomic size of the TM atom. For the adsorbed system, on the other hand, the adsorption height (*h*) for V (1.29 Å) and Cr (1.49 Å) adatoms is longer than Mn (1.05 Å), Fe (0.98 Å), and Co (0.94 Å) (Fig. 1(d)).A similar result of decreasing adsorption height has been reported for Fe, Co, and Ni adsorption on WSSe[40,45] and MoS_2[21]. This decreasing adsorption height (therefore X-S bond length) trend shows a close

System	Formation Energy (eV)	l_a (Å)	l_b (Å)	θ_a (°)	θ_b (°)	M_W (μB)†	M_X (μB)	$M_{S/Se}$ (μB)†	M_{Tot} (μB)
Pristine	0	2.42	2.53	84.14	79.48	0	0	0	0
V – Dopped	0.008	2.36	2.49	85.1	79.63	0.042	0.33	0.008/-0.008	0.88
Cr – Dopped	0.5	2.34	2.45	83.64	79.60	0	0	0	0
Mn – Dopped	1.4	2.33	2.41	85.89	76.45	0.025	1.02	-0.015/-0.02	1.0
Fe – Dopped	2.52	2.29*	2.43*	84.58**	79.74**	0.2	1.16	-0.01/-0.05	2.0
Co – Dopped	3.31	2.34*	2.63*	87.89**	79.89**	0.19	1.74	0.11/0.181	3.0

Table 1. Dopped System Formation Energy (E_f) bond length (l_a and, l_b), bond angles (θ_a and θ_b), and Magnetic moments for Tungsten (M_w), Transition Metal (M_x), Chalcogenide atom ($M_{S/Se}$), total Moment (M_{tot}). *Values are for two equal bond lengths. The third symmetry-breaking bond lengths (l_a/l_b) are Fe-S/Se = 2.32/2.46 and Co-S/Se = 2.41/2.44 **Average values are taken for three different angle values for the relaxed system. (Fe-S: θ_a (°) = 82.46,83.26,88.03, θ_b (°) = 78.06, 78.69, 83.04; Co-S: θ_a (°) = 83.85, 87.89, 87.96; θ_b (°) = 75.18, 79.89, 79.88)

System	Binding Energy (eV)	l_o (Å)	θ_o (°)/ h(Å)	M_W(μB)†	M_X(μB)	$M_{S/Se}$(μB)†	M_{Tot}(μB)
Pristine	0	2.42	---	0	0	0	0
V – Adsorbed	-2.21	2.31	93.77/1.28	0.215	3.08	0.009/0.005	5.0
Cr – Adsorbed	-0.96	2.41	86.64/1.49	0.12	4.18	0.01/0.01	6.0
Mn – Adsorbed	-1.52	2.21*	101.89**/1.05	0.083	2.94	-0.031/-0.013	3.0
Fe – Adsorbed	-1.98	2.16	103.16/0.98	0.092	1.911	-0.001/-0.019	2.0
Co – Adsorbed	-2.62	2.12*	103.43**/0.94	0.03	0.957	-0.006/-0.003	1.0

Table 2. Adsorbed System Formation Energy (E_f) bond length (l_o), bond angle(θ_o), adsorption height (h_o), and Magnetic moments for Tungston (M_w), Transition Metal (M_x), Chalcogenide atom($M_{S/Se}$), total Moment(M_{tot}). *Value is for two symmetrical bond lengths. The third symmetry-breaking bond lengths for Co-S and Mn-S are 2.16 and 2.23 Å, respectively **Average value is taken for three different angle values for the relaxed system (Mn-S: 99.45, 99.88, 106.35; Co-S: 102.317, 102.382, 105.606 deg) MW/S/Se values are for the nearest W/S/Se atoms from the dopant (adatom) TM element

relationship with the calculated binding energies and the crystal field splitting of *d* orbitals of TM atoms, as will be discussed in the next section.

Considering the symmetry of the system, for the case of Fe and Co doping, a symmetry-lowering distortion is observed where two chalcogenides are moved inwardly while one moves outward, reducing the system's symmetry from C_{3v} symmetry to C_s[61,62] (Table 1). Similarly, for the adsorbed system case, Mn and Co cause a symmetry-lowering distortion from C_{3v} symmetry to C_s (Table 2).

When checking the total magnetic moments, the extra valence holes/electrons added to the system give magnetic moments of 0.88, 0, 1, 2, and 3μB for V, Cr, Mn, Fe, and Co, respectively (Table 1). Whereas for the adsorbed X case, lone pairs from the X atoms give a total magnetic moment of 5, 6, 3, 2, and 1 μB for V, Cr, Mn, Fe, and Co, respectively (Table 2). The non-integer spin moment observed in doped V-WSSe hints at itinerant electrons mediating magnetic interaction[19,25,27]. Net spin moments for the nearest W and S/Se atoms are given in Tables 1 and 2. In both doped and adsorbed systems, higher magnetic moments on the nearest W atom are shown where longer X-S/Se bond lengths (l_a, l_b, and l_o) are observed. This reflects a weak *d-p-d* hybridization with the dopant, suggesting relatively localized states in defect 3*d*-orbitals[63]. On the other hand, shorter X-S/Se bond lengths align with relatively lower magnetic moments on the nearest W atoms, indicating a stronger *d-p-d* hybridization with the dopant/adsorbed atoms, as explained in the following section.

Electronic states and spatial distribution of spin states

Next, we closely follow the effects of these dopant/adsorbed atoms on the electronic and magnetic behavior of the host material. The introduction of magnetic dopant atoms disrupted structural symmetry (due to a change in local potential) and breaks time-reversal symmetry (due to exchange energy on local *d* states of TM atoms). The *d-p-d* hybridization between *TM-S/Se-W* atoms is then the connection that carries the magnetic disruption all the way to produce a spatial covering of spin states (i.e., the stronger the hybridization between *d*-orbitals $d_W - d_X$ and $p_{S/Se} - d_X$, the more spatially distributed spin biased states)[25].

Doped system

Figure 2 shows the *d*-orbital PDOS and spin density plot of the TM-atom doped WSSe system (Elemental projection of DOS is shown in Fig. S2). According to ligand field theory, the dopant atom's *d*-states split into a three-fold degenerate t_{2g} (d_{xz}, d_{yz}, d_{xy}) and twofold degenerate, e_g $\left(d_{z^2},\ d_{x^2-y^2}\right)$ orbital states in a perfect octahedral crystal field. Moreover, the structural distortion of octahedron makes the e_g state further split into A_1

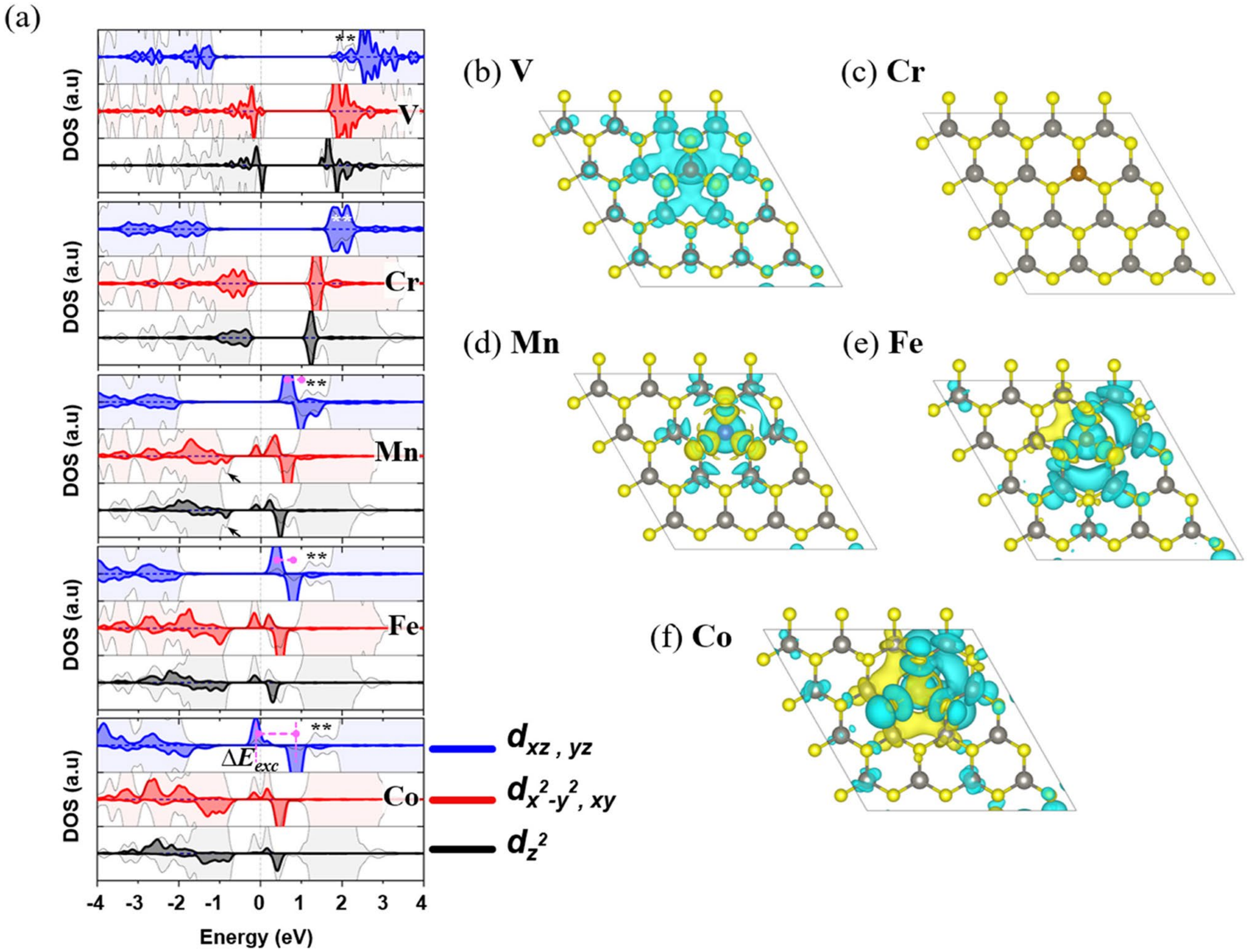

Figure. 2. (Color Online) X-WSSe Dopped System: (**a**) d-Orbital projected density of states of transition metal elements (X) and W atom. Thin-line shaded plots show respective d-orbitals $\left(d_{xz,\,yz},\ d_{x^2-y^2,\,xy},\ \text{and}\ d_{z^2}\right)$ of W atoms. Pink-colored horizontal dashed lines show the exchange energy within the *dxz* and *dyz* orbitals (ΔE*exc*). The asterisks ' ** ' denote the antibonding d *xz, yz* states of host W atom. (**b**)-(**e**) Spin density isosurface plots. Green and cyan colors represent positive and negative spin states. The isosurface value is set to 6E-4 e/Bohr^3. Note that states below Fermi energy in PDOS plots in (a) are to be related to the spin-density plots (**b**)–(**f**).

(d_{z^2}) and doubly degenerate E_2 $\left(d_{xy},\ d_{x^2-y^2}\right)$ states while the t_{2g} state is divided into E_1 (d_{xz}, d_{yz}) and E_2 (d_{xy}) as shown in Fig. 2(a)[64,65].

Regarding *p-d-p* hybridization with the host material, both V and Cr dopants show substantial *d-d* orbital overlap with the host material's respective *d*-orbitals (bonding and antibonding states). Since the $d_{xz,\,yz}$ orbitals are directed to the ligand atoms forming strong sigma bonding states, we can probe the bonding character and the magnetic interaction along these bonds[66]. The intensity of the overlap of these orbitals reflects the strength of the *d-p-d* hybridization, which lowers the potential disturbance of foreign elements (dopant atoms) to the system. Looking at the non-bonding states of $d_{xz,\,yz}$ orbitals in Fig. 2(a) (i.e., peaks marked with '**' in conduction band minimum within $d_{xz,\,yz}$ states), it is clearly shown that V and Cr-dopant show a strong overlap with the host materials' $d_{xz,\,yz}$ states. However, for Mn, Fe, and Co dopants, a decreasing overlap is observed, showing a decreasing *d-p-d* hybridization. Moreover, closely checking the exchange energies within defect $d_{xz,\,yz}$ orbitals, as we go from V, Mn, Fe, and Co, the exchange energy in $d_{xz,\,yz}$ orbitals increases from 0.03, 0.08, 0.21, and 0.58 eV (Fig. 2(a)) indicating a more localized defect state and therefore, a decreasing *d-p-d* hybridization with the host material. Note that the exchange energies in dopant atom will create the corresponding asymmetry in the unperturbed states (deep states/far below from E_f) at the valence band maximum of W atoms through strong *d-p-d* hybridization. If the strong *d-p-d* hybridization is observed, the deep states show spin asymmetry of states. For instance, for the Mn-doped WSSe, a small shoulder peak in VBM of $d_{x^2-y^2,\,xy}$ and d_{z^2} states around 0.9 eV shows induced spin-polarized states with an exchange energy of 0.16 eV (see arrow-pointed peaks in Fig. 2(a)) showing the possibilities of long-range order in Mn doped WSSe[6,67]. However, for Fe and Co dopants, there is no clear asymmetry in the deep states, showing less likely to form a spin-polarized band for long-range order.

Note that for Mn, Fe, and Co dopants, the extra electrons are in $d_{xy},\ d_{x^2-y^2},$ and d_{z^2} states and are pinned to the Fermi level with sharp peaks localized (see two peaks Fig. 2(a) below and above Fermi level in DOS plots).

To further assess orbital character and magnetic moment in dopped WSSe, we further checked the asymmetry of DOS in X/W atoms near and far states from Fermi and spin-density plots. Seemingly, a symmetrical spin up and down states are shown in V and Cr doped cases in $d_{xz,\ yz}$, states, while unsymmetrical DOS is observed for $d_{xz,\ yz}$, states in Mn, Fe and Co dopped cases. Whereas for the $A_1(d_{z^2})$ and $E_2\left(d_{xy},\ d_{x^2-y^2}\right)$, the unsymmetrical behavior is shown even for V and Cr doped cases, including all Mn Fe and Co dopped cases (Fig. 2(a)). This shows the different energy costs (i.e., exchange energy) for the states of *d*-orbitals inside the crystal field. The higher the exchange energy in defect *d*-states, the less dimer is formed through the *d*-*p*-*d* hybridization. Therefore, the exchange energy in each orbital hints the orbital overlap and magnetic moment character. For instance, in the V-doped case, the calculated *d*-orbital exchange energy (ΔE_{ex}) with a specific magnetic quantum l_m number shows $d_{xz,\ yz}$ = 0.03 eV, $d_{x^2-y^2,\ -xy}$ = 0.045 eV, d_{z^2} = 0.143 eV. This indicates relatively strongly localized d_{z^2} states than $d_{xz,\ yz}$ and $d_{x^2-y^2}$ orbitals. And thanks to strong hybridization through $d_{xz,\ yz}$ states, similar exchange energy is observed in W atoms therefore spin polarized states in d_{z^2} states of W atoms. This is confirmed with the spin density plot in Fig. 2(b), where a lobe on W atoms is directed along d_{z^2} states (*c*-axis), showing extra net spin moment along d_{z^2}.

Furthermore, the spatial distribution shown in the spin density plots Fig. 2(b-f) hints at the localized or itinerant carrier magnetic moments of the dopant or host material W and S/Se atoms[25–27,67]. For instance, the significant spatial distribution of spin density in V-WSSe in Fig. 2(b) supports abundant *d*-state DOS overlap between the V and W atoms shown in Fig. 2a. In contrast, a localized spin density is shown for other dopant materials, Mn, Fe, and Co (Fig. 2(d-f)), indicating less hybridized *d* defect states. Note that the increased spatial distribution of local spin density from Mn, Fe, to Co, only reflects an increasing size of magnetic moment (i.e., 1, 2, 3μB) from extra electrons as impurity level. Note that, for Cr-doped WSSe, as there are no spin-polarized states shown in PDOS plotting (Fig. 2(a)), zero spin density is shown in Fig. 2(c).

Moreover, an asymmetrical distribution of spin density in Fe and Co (Fig. 2(e) and (f)) reflects asymmetrical bond lengths around the dopant atom, as listed in Table 1. Therefore, for Fe and Co dopants, the structural symmetry breaking induces an AFM/FM interaction for the shorter/longer magnetic interaction distances between dopant-W and S(Se) atoms[57]. A similar result where asymmetrical spin density resulted from Fe adatom adsorbed on MoS_2S vacant is reported in[61]. On the other hand, all W and S/Se atoms are in a symmetrical FM interaction with the dopant V atoms, while for the Mn case, AFM/FM interaction exits for W/S(Se) atoms, respectively. Note that the magnetic interaction with the neighboring W/S(Se) atoms shows variation based on the empirical values of U for DFT + U results (Fig. S3).

Adsorbed system

Figure 3 shows the *d*-orbital PDOS and spin density plot of the TM-atom adsorbed on the S-face of WSSe, (Elemental projection of DOS is shown in Fig. S4). The *d*-orbitals of X adatom on WSSe do not split as much as it was for the doping case. Moreover, the *d*-states show reduced hybridization with the host material, as is shown in the slight overlapping of defect *d*-states and host *d*-states (Fig. 3(a)) compared to the doped system.

Moreover, in Fig. 3(a) a relatively narrow width of *d*-states and predominantly localized spin-density are shown for both V and Cr adatoms (Fig. 3(b) and (c)), which goes in line with the fact that both V and Cr have a relatively higher adsorption height. Whereas for adatoms of Mn, Fe, and Co, with relatively lower adsorption heights (Fig. 1(d)), *d*-orbitals are relatively dispersed (i.e., wider width DOS in Fig. 3(a)). For a given adatom, a more dispersed DOS for *d*-orbital confirms an integrated adatom, while a narrow and non-overlapped (with the host material) DOS reflects a less integrated adatom. Therefore, Mn, Fe, and Co integrate more with the host material WSSe than V and Cr adatoms. This, again, is in line with a decreasing exchange energy cost in $d_{xz,\ yz}$ orbital (orbital directed to the ligand S atoms). The $d_{xz,\ yz}$ orbital exchange energy cost for each adatom is 3.1, 4.2, 2.4, 1.2, and 0.6 for V, Cr, Mn, Fe, and Co, respectively (Fig. 3(a)). Moreover, compared to V and Cr adatoms, $d_{x^2-y^2,\ xy}$ orbital have larger overlap with $d_{x^2-y^2,\ xy}$ orbitals of W atom for Mn, Fe, and Co adatoms thereby increasing the binding energy and shortening the adsorption height. Therefore, a general simple picture is that the adsorption height reflects the bonding and, hence, *d*-*p*-*d* hybridization, which directs electronic and magnetic properties.

Moreover, here we need to consider the ionic radii effect as we go from V^{+5}, Cr^{+6}, Mn^{+1}, Fe^{+2} to Co^{+3}(0.4, 0.35, 0.7, 0.67, 0.64)[68], which dictates the spatial overlap of orbitals and localization of bonding electrons. For a given adatom element (i.e., with the same electronegativity), the smaller the atomic size, the lower the overlap of orbitals and less hybridization[68]. Therefore, a general picture can be deducted considering the ionic radii together with adatom's electronegativity (that can lead to the absorption height) and hence dictates magnetic exchange interactions distances (i.e., between TM-W), which resulted in FM (V and Cr) and AFM (Mn, Fe, and Co) magnetic exchange interactions. This can be understood as when the shared electrons hop between sites within a shorter distance, an AFM interaction tends to lower energy. In contrast, in the more extended interaction, the FM interaction favors lowering the system's energy[63,69]. For the V-WSSe case, for instance, the FM spin interaction exists for both interactions between the V -S/Se and the V-W atoms (shown as the same color in Fig. 3(b)). In the Mn-WSSe doped case, the Mn-W interaction shows FM, while Mn-S/Se shows AFM interactions (shown as the different colors in Fig. 3(d))[70].

Magnetic Anisotropy Energy (MAE)

In the following section, we systematically presented the MAE results, thereby presenting the easy axis and its relation with the *d*-states of a magnetically 'seasoned' WSSe. Figure 4. shows the MAE results for both doping (Fig. 4(a)) and adsorbed (Fig. 4(b)) systems for which the easy axis lies mainly along the *c*-axis for both systems.

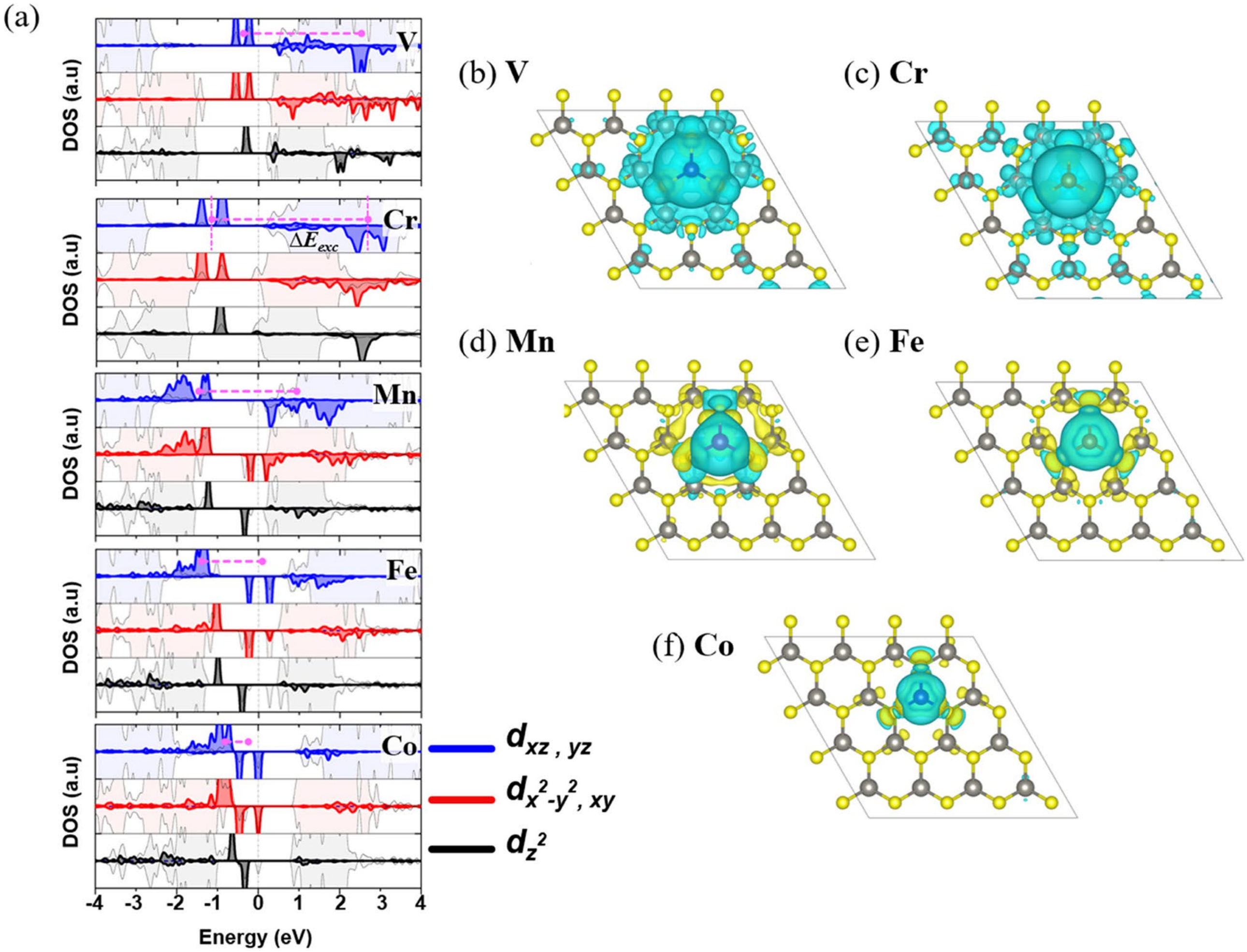

Figure. 3. (Color Online) WSSe-X Adsorbed System: (a) d-Orbital projected density of states of transition metal elements (X) and W atom. Thin-line shaded plots show respective d-orbitals $\left(d_{xz,\ yz},\ d_{x^2-y^2,\ xy},\ \text{and}\ d_{z^2}\right)$ of W atoms. Pink-colored horizontal dashed lines show the exchange energy within the d *xz* and d *yz* orbitals (ΔE *exc*). The asterisks ' ** ' denote the antibonding d *xz*, *yz* states of host W atom. (b)-(e) Spin density iso-surface plots. Green and cyan colors represent positive and negative spin states. The isosurface value is set to 6E-4 e/Borh^3. Note that states below Fermi energy in PDOS plots in (a) are to be related to the spin-density plots (b) –(f).

For V and Cr adsorbed cases, however, the easy axis lies in the *a*-*b* plane. This difference can be roughly attributed to the adsorption height (*h*), in which both V and Cr atoms have relatively longer adsorption heights than the rest of the adatoms. This result is in line with ample reports where the adsorption height influences a switch in the easy axis of the adsorbed system[71–74]. However, the origin of MAE in a crystal can be understood by treating the SOC as a perturbation in the crystal field of the system. Therefore, a clear SOC and orbital contribution map is essential.

Magnetic anisotropy is mainly dictated by two significant contributions: (1) Orbital moment anisotropy (spin-conserving) and (2) Magnetic dipole moment (spin-flipping)[75,76]. Neglecting the spin-flip term (because of low proportions of either majority or minority states near the Fermi level, (Figs. 2(a) and 3(a)), accounting SOC in the doped/adsorbent WSSe, lowers the energy of a system by, $H = -\xi\,\widehat{L}\cdot\widehat{S} = -\widehat{S}\cdot\Lambda\cdot\widehat{S} = DS + E\left(S_x^2 - S_y^2\right)$ [76,77] (here ξ is SOC constant), where Λ is the tensor of the SOC, $D = \Lambda_{zz} - \frac{(\Lambda_{xx}+\Lambda_{yy})}{2}$ and $E = \frac{(\Lambda_{xx}-\Lambda_{yy})}{2}$

. Where, $\Lambda_{xx}, \Lambda_{yy}$, Λ_{zz} are the diagonal elements of SOC tensor given by

$$\Lambda_{ii} = \xi^{2}\sum_{nm}\frac{\left\langle m|\widehat{L}_i|n\right\rangle\left\langle m|\widehat{L}_i|n\right\rangle}{E_n - E_m} \tag{1}$$

where $\widehat{L}_i = \widehat{L}_x, \widehat{L}_y, \widehat{L}_z$ stands for three anisotropic components of the orbital moment operator $\widehat{\boldsymbol{L}}$, $|\mathrm{n}>$ and $\mathrm{E_n}$ ($|\mathrm{m}>$ and $\mathrm{E_m}$) are the wavefunctions and the corresponding eigen-energies of the occupied

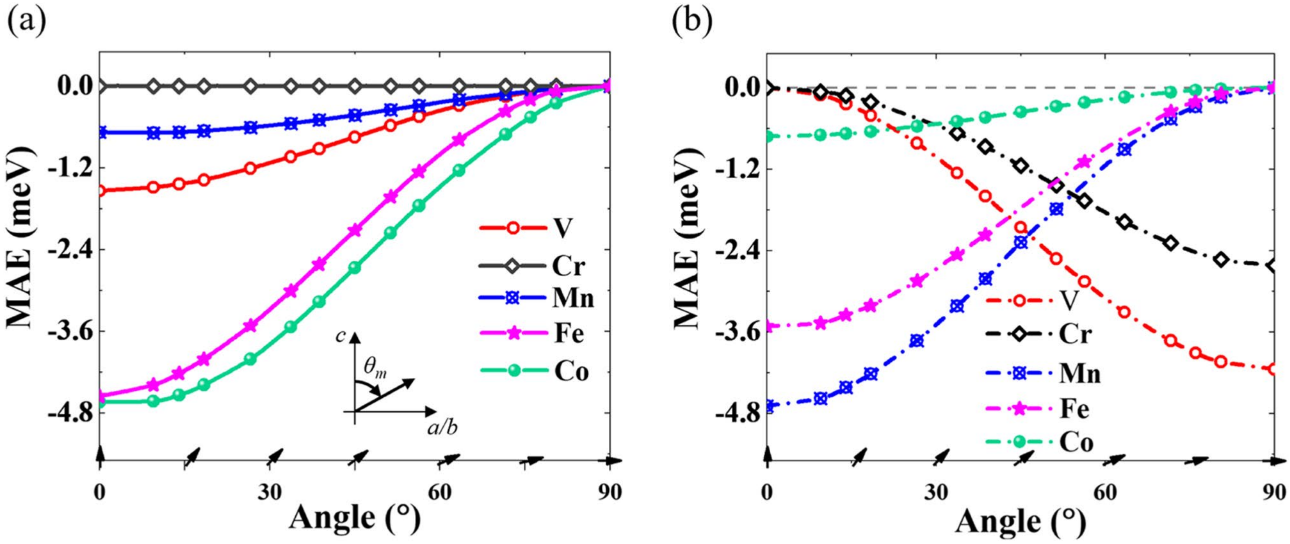

Figure. 4. (Color Online) Magnetic Anisotropy in (**a**) Dopped and (**b**) Adsorbed System. Note that in the Cr-dopped system, there is no magnetism, as shown in Fig. 2(c). Inset in (a) shows angle θ_m swept from the c-axis to the a-b plane. Note that a relative energy value is displayed, i.e., the lowest number shows the easy axis. The arrows at the horizontal axis showing spin directions are a guide to the eye.

(unoccupied) electron states, respectively (i.e., near Fermi states). The above equation indicates that the gap in the localized electronic states around Fermi energy (i.e., denominator energy values, occupied and unoccupied states) is inversely related to the calculated unquenched orbital moments[61,75,77,78].

To understand the relationship between calculated MAE results and *d*-states, *d*-orbital resolved MAE is a suitable probing method. In the X-WSSe system, the diagonal elements of SOC tensor Λhave the unquenched orbital moment operators $< d_{xy}|\boldsymbol{Lz}|d_{x^2-y^2} >$ as its primary contributor (Figs. S5 and S6). According to Eq. (1), this can be reasoned as; since d_{xy} and $d_{x^2-y^2}$ orbitals are dominant near Fermi energy (Figs. 2(a) and 3(a)) the denominator in Eq. (1), ($E_n - E_m$), will have a lower value (i.e., a small energy gap), thereby mounting the contribution of $|\boldsymbol{L}_z|$ operator. In Fig. 5, a matrix representation of two dominant operators $|\boldsymbol{L}_z|$ and $|\boldsymbol{L}_x|$ in both doped (Fig. 5(a) and (c)) and adsorbed (Fig. 5(b) and (d)) systems is shown. In all TM elements, the nearest W atom in the adsorbed case contributes more to MAE than the doped case. Moreover, the contribution of X and W atoms is directed to the same easy axis except for Cr-adatom, which in both $|\boldsymbol{L}_z|$ and $|\boldsymbol{L}_x|$ operators opposing contribution from X and W atom is shown. This is reflected in a reduced total MAE shown in Fig. 4(b) compared to the V-adatom. For the V-WSSe adsorbed system, on the other hand, the contribution of $|\boldsymbol{L}_z|$ and $|\boldsymbol{L}_x|$ operators oppose each other, showing a possible tunability of MAE via external stimuli.

Furthermore, a local distortion of symmetry in both dopped (Fe and Co) and adsorbed systems (Mn and Co) is shown to enhance the system's MAE by removing the degenerate states of E_1 and E_2 [19,34]. By removing the degenerate d_{xy} and $d_{x^2-y^2}$ states, the energy gap denominator in Eq. (1) decreases further, enlarging the SOC tensor's diagonal elements[75,79]. Moreover, the density of states near fermi gets enlarged which will cause the MAE increase according to Eq. (1).

However, the easy axis switch (i.e., from doped to adsorbed system) of V atom and in-plane easy axis in Cr-adsorbed can be explained with the magnetic spin-flip term (i.e., quadrupole term, or magnetic dipole moment) included in the Hamiltonian of SOC[75,76,80] as given by:

$$H^{SOC} = \frac{\xi}{4}\Delta\, m_{orb} + \frac{21}{2}\frac{\xi^2}{\Delta_{exc}} m_T \tag{2}$$

Here, Δm_{orb} and m_T are the orbital moment anisotropy and magnetic dipole moment, respectively, and ξ and Δ_{exc} are the SOC constant and exchange splitting of the corresponding materials, respectively. The first and second terms in Eq. (2) are the spin-conserving and spin-flip terms, respectively. According to Bruno's model (which neglects the spin-flip term in Eq. (2)), MAE is proportional to the difference between orbital moments along the easy and hard directions[77,81,82]. However, the orbital moment anisotropy remains positive in all the adatoms, as shown in Fig. S7(b). Therefore, MAE's other contribution comes from the spin-flip term. The spin-flip term of MAE is described by the magnetic dipole moment, indicating that the origin of the perpendicular MAE can be attributed to the shape of spin density rather than the orbital moment anisotropies[77,79]. This aligns with the spin density shown in Fig. 3(b) and (c), where a significant oblate spin distribution is seen around adatoms V and Cr. Moreover, as shown in Fig. 3(a), only for the adsorbed V and Cr atom cases, there are no same-spin d_{xy} and $d_{x^2-y^2}$ states below and above Fermi energy, while there are plenty of opposite-spin d_{xy} and $d_{x^2-y^2}$ states near Fermi energy. This will cause the spin-conserving term to diminish. Therefore, the flip term in the Hamiltonian dominates MAE in which the contribution favors the *a*-*b*plane easy axis[75,77].

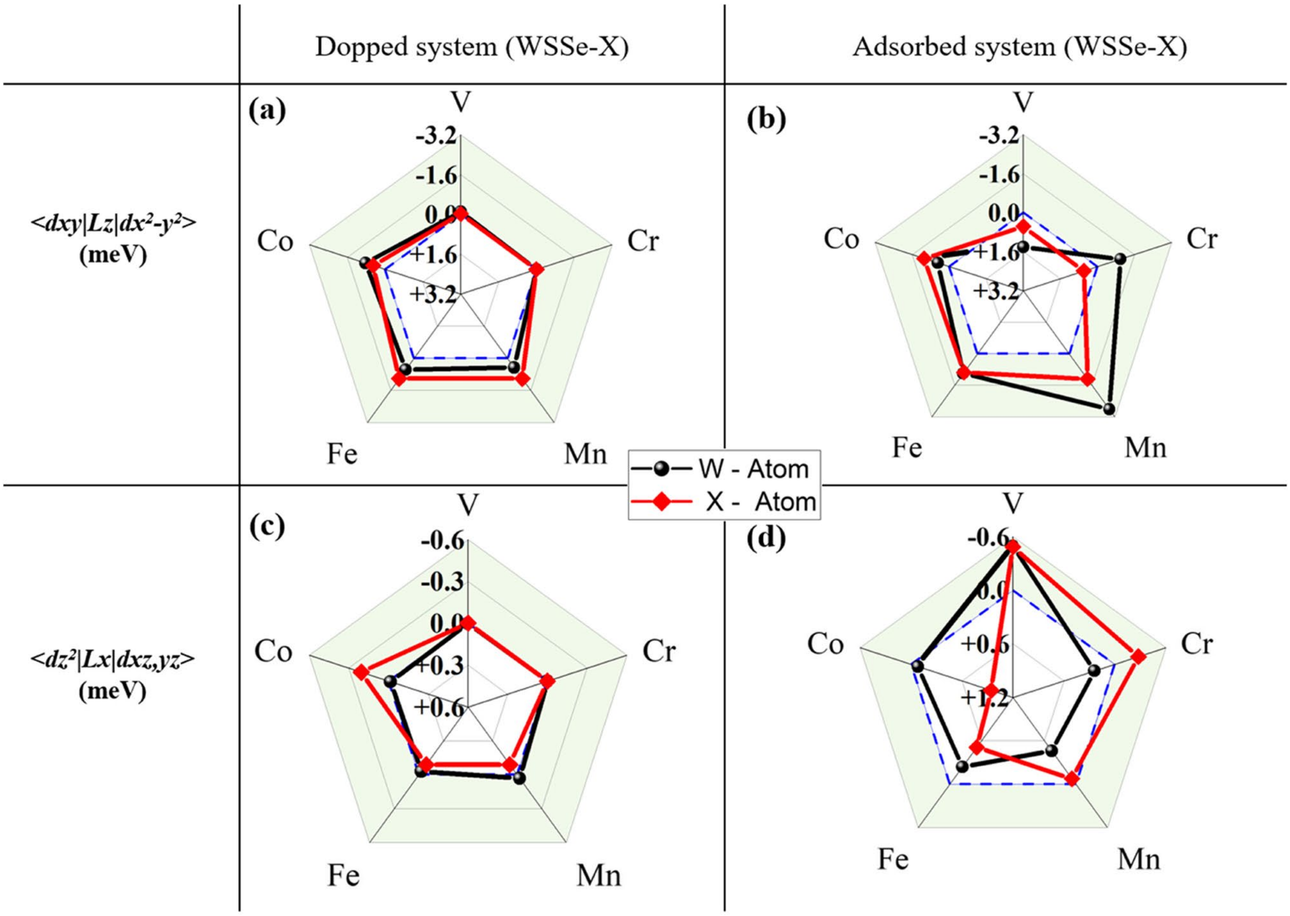

Figure. 5. (Color Online) Orbital resolved MAE matrix for X and nearest W atoms. Contribution of two unquenched orbital operators $|L_z|$ and $|L_x|$ in Dopped (a, c) and Adsorbed (b, d) WSSe-X system. (a) and (b) $< d_x|Lz|d_{x^2-y^2} >$/ (c) and (d) $<d_z^2|L_x|d_{xz,\, yz}>$. The blue dashed line represents a zero MAE value. Note that for both $|L_z|$ and $|L_x|$ operators, positive/negative sign contribution stabilizes the easy axis along the c-axis/a-b plane.

Consequently, we conclude that for both V and Cr-adsorbed systems, the finite quadrupole-like orbital distortion through spin-flipped electron hopping is dominant and originates from relatively strongly localized *d*-states of V and Cr ions[79].

Considering the elemental contribution of MAE, we have found that the heavy W atom in the host material has a significant contribution in both doped and adsorbed system cases (Fig. 5). Furthermore, site-dependent MAE plots in V and Co systems show that W atoms' contribution falls as we move away from the dopant/adsorbed atom (Fig. S8).

Table 3 shows a representative summary table of the relationship between atomic (ionic) radii, stability of the system (formation energy/binding energy), and electronegativity of the dopant (adatom). Considering the stability of the system, V-doped and Co-adsorbed systems are comfortably formed (i.e., very little energy required for V-dopant and larger binding energy for Co adatom), whereas for induced MAE value and *c*-axis direction, Co-doped and Mn-adsorbed possess the highest values along the *c*-axis. On the other hand, for long-range magnetic order, the V-doped system is best as observed in well-overlapped DOS and spatial distribution of spin density, which shows strong *d-p-d*hybridization with host WSSe while Mn-dopped system also shows a substantial overlap of DOS, matching to the possible long-range magnetic order reported[67].

Conclusion

In summary, we have systematically studied the effects of defect states of transition metal atoms (V, Cr, Mn, Fe, and Co) on doped and adsorbent Janus WSSe on the basis of the first-principles calculations. Throughout the study, we focused on three main points: (1) structural parameters (i.e., bond length and adsorption heights), (2) *d-p-d* hybridization and defect states, and (3) magnetic anisotropy. We have tried to elucidate the relationship between these three aspects in light of magnetic exchange interactions and spatial spin density distribution. Spatial spin-density distribution, which is directly related to a long-range magnetic ordering, results from a well-integrated adatom/dopant and, therefore, the induced slight onsite exchange energy in W atoms. Considering the relationship of spin-density distribution with MAE, the MAE for both dopant and adatom is mainly contributed

Element			Doped system				Adsorbed system			
	$\dot{r}$ (Å)*	$\Delta\chi^{\dagger}$ (eV)	*$\Delta l_a/l_b$(%)*	Stability (E_f) *(eV)*	*d-p-d ** (Spin-induced in W atoms)*	*MAE (meV)*	*h(Å)*	Stability (E_b) *(eV)*	*d-p-d ** (Spin-induced in W atoms)*	*MAE (meV)*
W	0.4	0.00	0.0/0.0	--	--	--	--	--	--	--
V	0.4	3.20	-2.5/-1.6	0.008	Very Good	-1.54	1.28	-2.21	Very Poor	+4.15
Cr	0.35	3.27	-3.3/-3.2	0.5	Excellent	-0	1.49	-0.96	Poor	+2.62
Mn	0.7	3.34	-3.7/-4.7	1.4	Good	-0.68	1.05	-1.52	Satisfactory	-4.69
Fe	0.67	3.42	-5.3/-3.9	2.52	Poor	-4.56	0.98	-1.98	Poor	-3.52
Co	0.64	3.49	-3.4/+3.9	3.31	Poor	-4.64	0.94	-2.62	Satisfactory	-0.72

Table 3. Comparative summary table. An inclusive Doped and Adsorbed System structural, d-p-d hybridization (d-p-d), stability, and MAE results in comparison. Ionic radii ($\dot{r}$), Difference in Electronegativity ($\Delta\chi$) = $(\chi)_W$- $(\chi)_X$, Bond length difference from the host W-S/Se bond length (%) Δl_b / Δl_a, Stability measured as E_f or E_b for doped and adsorbed system respectively. Note that d-p-d hybridization (d-p-d) is expressed in a qualitative word based on V-WSSe results as a base. * With their Respective charges W^{+4}, V^{+3}, Cr^{+4}, Mn^{+1}, Fe^{+2}, and Co^{+3}, Ref[68]. † Ref[60]. **(Qualitative description used only for comparison within each column, and are based on DOS overlap and Spin Density plot in Figs. 2(a) and 3(a)).

from the spin-conserving term of SOC Hamiltonian (which is insensitive to spin-density distribution); however, for polarized lobe spin-density distribution, the spin-flip term (i.e., spin dipole moment) becomes significant, and dictates the easy axis, as was observed in V and Cr adatoms. From our results, we have shown that:

(1) On the doped system, the size of ionic size and the relative electronegativity of the atom dictate the *d-p-d* hybridization (and, therefore, the splitting of defect states) and, consequently, the stability of the doped system. On the other hand, the symmetry breaking of X-S/Se bonds (from C_{3v} symmetry to C_s) leads to an enhanced MAE.
(2) In the adsorbed system, the adsorption height, which is governed by the atomic size of the adatoms, dictates the position of defect states and, therefore, the stability of the adsorbed system. Again, the symmetry breaking in the X-S/Se bond leads to enhanced MAE, while the easy axis is shown to be influenced by spin density distribution.

The finding in this theoretical report serves as a guide for further exploration of the magnetic properties of doped/adsorbent WSSe and other 2D materials to search for long-range magnetic orderings.

Data availability

The datasets used and/or analysed during the current study available from the corresponding author on reasonable request.

Received: 23 July 2024; Accepted: 28 October 2024

References

1. Dietl, T. & Ohno, H. Dilute ferromagnetic semiconductors: physics and spintronic structures. *Rev. Mod. Phys.* **86**, 187–251 (2014).
2. Sato, K. et al. First-principles theory of dilute magnetic semiconductors. *Rev. Mod. Phys.* **82**, 1633–1690 (2010).
3. Dietl, T. A ten-year perspective on dilute magnetic semiconductors and oxides. *Nat. Mater.* **9**, 965–974 (2010).
4. Dietl, T. Ferromagnetic semiconductors. *Semicond. Sci. Technol.* **17**, 377–392 (2002).
5. Akai, H. Ferromagnetism and Its Stability in the Diluted Magnetic Semiconductor (In, Mn)As. *Phys. Rev. Lett.* **81**, 3002–3005 (1998).
6. Dobrowolska, M. et al. Controlling the Curie temperature in (Ga,Mn)As through location of the Fermi level within the impurity band. *Nat. Mater.* **11**, 444–449 (2012).
7. Heinzen, D. J. et al. Zener Model Description of Ferromagnetism in Zinc-Blende Magnetic Semiconductors. *Chem. Phys. Lett.* **284**, 1019–1022 (2000).
8. Gong, C. et al. Discovery of intrinsic ferromagnetism in two-dimensional van der Waals crystals. *Nature*. **546**, 265–269 (2017).
9. Fei, Z. et al. Two-dimensional itinerant ferromagnetism in atomically thin Fe3GeTe2. *Nat. Mater.* **17**, 778–782 (2018).
10. Junho et al. Nearly room temperature ferromagnetism in a magnetic metal-rich van der Waals metal. *Sci. Adv.* **6**, 1–9 (2020).
11. Bonilla, M. et al. Strong room-temperature ferromagnetism in VSe2 monolayers on van der Waals substrates. *Nat. Nanatechnol. 2018*. **13:4 13**, 289–293 (2018).
12. Li, H., Ruan, S. & Zeng, Y. J. Intrinsic Van Der Waals Magnetic Materials from Bulk to the 2D Limit: New Frontiers of Spintronics. *Adv. Mater.* **31**, 1–34 (2019).
13. Gibertini, M., Koperski, M., Morpurgo, A. F. & Novoselov, K. S. Magnetic 2D materials and heterostructures. *Nat. Nanotechnol.* **14**, 408–419 (2019).
14. Balan, A. P. et al. Non-van der Waals quasi-2D materials; recent advances in synthesis, emergent properties and applications. *Mater. Today*. **58**, 164–200 (2022).
15. Wu, H. et al. Strong intrinsic room-temperature ferromagnetism in freestanding non-van der Waals ultrathin 2D crystals. *Nat. Commun.* **12**, 8–15 (2021).
16. Liu, X., Gebredingle, Y., Guo, X., Zhang, F. & Kim, N. Thickness-dependent crystal structure, synthesis, and magnetism of thin film chromium chalcogenides: A review. *Adv. Funct. Mater.* Preprint at. https://doi.org/10.1002/adfm.202316834 (2024).

17. Fang, Q. et al. Structural stability and magnetic-exchange coupling in Mn-doped monolayer/bilayer MoS2. *Phys. Chem. Chem. Phys.* **20**, 553–561 (2017).
18. Kochat, V. et al. Re doping in 2D transition metal dichalcogenides as a new route to tailor structural phases and induced magnetism. *Adv. Mater.* **29**, 1703754 (2017).
19. Yun, S. J. et al. Ferromagnetic order at room temperature in monolayer WSe2 semiconductor via vanadium dopant. *Adv. Sci.* **7**, 1903076 (2020).
20. Coelho, P. M. et al. Room-temperature ferromagnetism in MoTe 2 by post-growth incorporation of vanadium impurities. *Adv. Electron. Mater.* **5**, 1900044 (2019).
21. Yue, Q., Chang, S., Qin, S. & Li, J. Functionalization of monolayer MoS2 by substitutional doping: A first-principles study. *Phys. Lett. Sect. A: Gen. At. Solid State Phys.* **377**, 1362–1367 (2013).
22. Andriotis, A. N. & Menon, M. Tunable magnetic properties of transition metal doped MoS2. *Phys. Rev. B Condens. Matter Mater. Phys.* **90**, 125304 (2014).
23. You, S., Kim, H. & Kim, N. Valley filtering using magnetic proximity effect in monolayer WS2. *Phys. E Low Dimens Syst. Nanostruct.* **162**, 115975 (2024).
24. Tiwari, S., Van de Put, M. L., Sorée, B. & Vandenberghe, W. G. Magnetic order and critical temperature of substitutionally doped transition metal dichalcogenide monolayers. *NPJ 2D Mater. Appl.* **5**, 54 (2021).
25. Duong, D. L., Yun, S. J., Kim, Y., Kim, S. G. & Lee, Y. H. Long-range ferromagnetic ordering in vanadium-doped WSe2 semiconductor. *Appl. Phys. Lett.* **115**, 242406 (2019).
26. Duong, D. L., Kim, S. G. & Lee, Y. H. Gate modulation of the long-range magnetic order in a vanadium-doped WSe2semiconductor. *AIP Adv.* **10**, 065220 (2020).
27. Song, B. et al. Evidence of itinerant holes for long-range magnetic order in the tungsten diselenide semiconductor with vanadium dopants. *Phys. Rev. B.* **103**, 094432 (2021).
28. Zhang, J. et al. Janus Monolayer Transition-Metal Dichalcogenides. *ACS Nano*. **11**, 8192–8198 (2017).
29. Lu, A. Y. et al. Janus monolayers of transition metal dichalcogenides. *Nat. Nanotechnol*. **12**, 744–749 (2017).
30. Zhang, L. et al. Recent advances in emerging Janus two-dimensional materials: From fundamental physics to device applications. *J. Mater. Chem. Mater.* **8**, 8813–8830 (2020).
31. Li, R., Cheng, Y. & Huang, W. Recent progress of Janus 2D transition metal chalcogenides: From theory to experiments. *Small*. **14**, 1802091 (2018).
32. Yao, Q. F. et al. Manipulation of the large Rashba spin splitting in polar two-dimensional transition-metal dichalcogenides. *Phys. Rev. B.* **95**, 165401 (2017).
33. Guan, Z. & Ni, S. Predicted 2D ferromagnetic Janus VSeTe monolayer with high Curie temperature, large valley polarization and magnetic crystal anisotropy. *Nanoscale*. **12**, 22735–22742 (2020).
34. Er, D. et al. Prediction of Enhanced Catalytic Activity for Hydrogen Evolution Reaction in Janus Transition Metal Dichalcogenides. *Nano Lett.* **18**, 3943–3949 (2018).
35. Ding, Y. et al. First-Principles Predictions of Janus MoSSe and WSSe for FET Applications. *J. Phys. Chem. C*. **124**, 21197–21206 (2020).
36. Cui, Z. et al. WS2 and WSSe bilayer with excellent carrier mobility and power conversion efficiency. *Mater. Sci. Semicond. Process.* **167** (2023).
37. Ju, L., Bie, M., Tang, X., Shang, J. & Kou, L. Janus WSSe Monolayer: An Excellent Photocatalyst for Overall Water Splitting. *ACS Appl. Mater. Interfaces*. **12**, 29335–29343 (2020).
38. Feng, S. et al. First-principles study on electronic and optical properties of van der Waals heterostructures stacked by g-ZnO and Janus-WSSe monolayers. *Appl. Surf. Sci.* **604**, 154620 (2022).
39. Ju, L. et al. NO2 Physical-to-chemical adsorption transition on janus WSSe monolayers realized by defect introduction. *Molecules*. **28**, 1644 (2023).
40. Guo, J. X. et al. Janus WSSe monolayer adsorbed with transition-metal atoms (Fe, Co and Ni): excellent performance for gas sensing and CO catalytic oxidation. *Appl. Surf. Sci.* **565**, 150558 (2021).
41. Ahmad, S. et al. First principles study of the adsorption of alkali metal ions (Li, Na, and K) on Janus WSSe monolayer for rechargeable metal-ion batteries. *Appl. Surf. Sci.* **632**, 157545 (2023).
42. Zhang, J. et al. Two-dimensional Sc2CF2/WSSe van der Waals heterostructure for water splitting: A first-principles study. *J. Phys. Chem. Solids*. **185**, 111757 (2024).
43. Zhao, X. W. et al. Transition-metal doping/adsorption induced valley polarization in Janus WSSe: First-principles calculations. *Appl. Surf. Sci.* **490**, 172–177 (2019).
44. She, X. C. et al. Tunable valley polarization in Janus WSSe by magnetic proximity coupling to a CrI3layer. *Phys. Chem. Chem. Phys.* **23**, 18182–18188 (2021).
45. Chen, K. et al. Manipulation of the magnetic properties of Janus WSSe monolayer by the adsorption of transition metal atoms. *Nanoscale Res. Lett.* **16**, 104 (2021).
46. Hu, S. et al. First-principles investigations upon Pd-decorated Janus WSSe monolayer for sensing typical gases in overload dry-type transformers. *Comput. Theor. Chem.* **1229**, 114344 (2023).
47. Srivastava, M., Pandey, B. P., Mishra, N. & Kumar, S. Investigation of electronic stabilities and properties of Mn-doped Janus WSSe monolayer. *Comput. Condens. Matter*. **31**, e00677 (2022).
48. Ye, H. et al. Exploration of Pt-doped Janus WSSe monolayer as a typical gas sensor for condition assessment in XLPE cables. *Chem. Phys. Lett.* **832**, 140880 (2023).
49. Kresse, G. Efficient iterative schemes for ab initio total-energy calculations using a plane-wave basis set. *Phys. Rev. B*. **54**, 11169–11186 (1996).
50. Perdew, J. P., Burke, K. & Ernzerhof, M. Generalized gradient approximation made simple. *Phys. Rev. Lett.* **77**, 3865–3868 (1996).
51. Dudarev, S. & Botton, G. Electron-energy-loss spectra and the structural stability of nickel oxide: An LSDA + U study. *Phys. Rev. B Condens. Matter Mater. Phys.* **57**, 1505–1509 (1998).
52. Chai, J., Ming, C. & Sun, Y. Y. Decomposed defect formation energy for analysis of doping process: The case of n-type and p-type doping of β-FeSi2. *Appl. Phys. Lett.* **123**, 252103 (2023).
53. Gao, W., Zhao, J. & Chelikowsky, J. R. Out-of-plane polarization and topological magnetic vortices in multiferroic CrPSe3. *Phys. Rev. Mater.* **6**, L101402 (2022).
54. Hendrik, J. & Monkhorst Pack. Special points for Brillonin-zone integrations. *Phys. Rev. B*. **13**, 5188–5192 (1976).
55. Ju, L., Tang, X., Li, J., Shi, L. & Yuan, D. Breaking the out-of-plane symmetry of Janus WSSe bilayer with chalcogen substitution for enhanced photocatalytic overall water-splitting. *Appl. Surf. Sci.* **574**, 151692 (2022).
56. Fang, M. & Yang, E. H. Advances in two-dimensional magnetic semiconductors via substitutional doping of transition metal dichalcogenides. *Materials*. **16**, 3701 (2023).
57. Zhao, X., Chen, P. & Wang, T. Controlled electronic and magnetic properties of WSe2 monolayers by doping transition-metal atoms. *Superlattices Microstruct.* **100**, 252–257 (2016).
58. Oura, K., Lifshits, V. G., Saranin, A. A., Zotov, A. V. & Katayama, M. *Surface Science-An Introduction* (Springer, 2003).
59. Huang, J. et al. Chemisorption of NO2 to MoS2 Nanostructures and its Effects for MoS2 Sensors. *ChemNanoMat*. **5**, 1123–1130 (2019).

60. Ghosh, D. C. & Chakraborty, T. Gordy's electrostatic scale of electronegativity revisited. *J. Mol. Struct. (Thoechem)*. **906**, 87–93 (2009).
61. Cong, W. T., Tang, Z., Zhao, X. G. & Chu, J. H. Enhanced magnetic anisotropies of single transition-metal adatoms on a defective MoS2 monolayer. *Sci. Rep.* **5**, 9361 (2015).
62. Xu, B. et al. First-principles study of magnetic properties and electronic structure of 3d transition-metal atom-adsorbed SnSSe monolayers. *Phys. Chem. Chem. Phys.* **26**, 4231–4239 (2024).
63. Zener, C. Interaction Between the d Shells in the Transition Metals*. *Phys. Rev.* **81**, 440–444 (1951).
64. Chhowalla, M. et al. The chemistry of two-dimensional layered transition metal dichalcogenide nanosheets. *Nat. Chem.* **5**, 263–275 (2013).
65. Mattheiss, L. F. Band Structures of Transition-Metal-Dichalcogenide Layer Compounds. *Phys. Rev. B*. **8**, 3719–3740 (1973).
66. Liu, G., Bin, Shan, W. Y., Yao, Y., Yao, W. & Xiao, D. Three-band tight-binding model for monolayers of group-VIB transition metal dichalcogenides. *Phys. Rev. B Condens. Matter Mater. Phys.* **88**, 039901 (2013).
67. Mishra, R., Zhou, W., Pennycook, S. J., Pantelides, S. T. & Idrobo, J. C. Long-range ferromagnetic ordering in manganese-doped two-dimensional dichalcogenides. *Phys. Rev. B*. **88**, 144409 (2013).
68. Boris, K., Vainshtein, Vladimir, M., Fridkin, Vladimir, L. & Indenbom *Structure of Crystals (Modern Crystallography 2)* (Springer, 2000). https://doi.org/10.1007/978-3-642-57254-8
69. Jang, S. W., Jeong, M. Y., Yoon, H., Ryee, S. & Han, M. J. Microscopic understanding of magnetic interactions in bilayer CrI3. *Phys. Rev. Mater.* **3**, 1–6 (2019).
70. Wu, M. et al. Electronic structures, magnetic properties and band alignments of 3d transition metal atoms doped monolayer MoS2. *Phys. Lett. Sect. A: Gen. At. Solid State Phys.* **382**, 111–115 (2018).
71. Guan, X., Zhang, Y., Long, X., Zhu, G. J. & Cao, J. Tuning magnetocrystalline anisotropy by controlling the orbital electronic configuration of two-dimensional magnetic materials. *Nanoscale Adv.* **5**, 2501–2507 (2023).
72. Yang, G. et al. Tuning the crystalline field leads to giant regulated perpendicular magnetic anisotropy by depositing Bi atom onto the MgO surface. *Phys. E Low Dimens Syst. Nanostruct.* **136**, 115039 (2022).
73. Li, Z., Chen, B., Shan, S. & Zhang, Y. Magnetization reversal of perpendicular magnetic anisotropy regulated by ferroelectric polarization in CoFe3N/BaTiO3 heterostructures: first-principles calculations. *RSC Adv.* **13**, 9924–9931 (2023).
74. Odkhuu, D. Giant perpendicular magnetic anisotropy of an individual atom on two-dimensional transition metal dichalcogenides. *Phys. Rev. B*. **94**, 060403 (2016).
75. Van Der Laan, G. Microscopic origin of magnetocrystalline anisotropy in transition metal thin films. *J. Phys. : Condens. Matter*. **10**, 3239–3253 (1998).
76. Wang, D. S., Wu, R. & Freeman, A. J. First-principles theory of surface magnetocrystalline anisotropy and the diatomic-pair mode. *Phys. Rev. B*. **47**, 14932–14947 (1993).
77. Miura, Y. & Okabayashi, J. Understanding magnetocrystalline anisotropy based on orbital and quadrupole moments. *J. Phys. Condens. Matter*. **34**, 1–18 (2022).
78. Yang, B., Zhang, X., Yang, H., Han, X. & Yan, Y. Nonmetallic Atoms Induced Magnetic Anisotropy in Monolayer Chromium Trihalides. *J. Phys. Chem. C*. **123**, 691–697 (2019).
79. Okabayashi, J. et al. Detecting quadrupole: a hidden source of magnetic anisotropy for Manganese alloys. *Sci. Rep.* **10**, 9744 (2020).
80. Stöhr, J. & Siegmann, H. C. *Magnetism From Fundamentals to Nanoscale Dynamics* (Springer-, 2006).
81. Bruno, P. Tight-binding approach to the orbital magnetic moment and magnetocrystalline anisotropy of transition-metal monolayers. *Phys. Rev. B*. **39**, 865 (1989).
82. Yan, S. et al. Role of exchange splitting and ligand-field splitting in tuning the magnetic anisotropy of an individual iridium atom on Ta S 2 substrate. *Phys. Rev. B*. **103**, 224432 (2021).

Author contributions

Y.G. H. K. and N.K. conceived the computational study. Y.G. performed the DFT calculations. Y.G. analyzed the results and interpreted the data. H. K. and N.K. provided guidance and supervision. N.K. coordinated the research project. All authors contributed to writing and reviewing the manuscript.

Funding

This work was supported by the Basic Science Research Program through the National Research Foundation of Korea (NRF), funded by the Ministry of Science and ICT (Grant No.~NRF-2023R1A2C1003489), and the Creative Challenge Research Program through the National Research Foundation of Korea (NRF) funded by the Ministry of Science and ICT (Grant No.~ RS-2023-00241215).

Declarations

Competing interests

The authors declare no competing interests.

Additional information

Supplementary Information The online version contains supplementary material available at https://doi.org/10.1038/s41598-024-77938-x.

Correspondence and requests for materials should be addressed to Y.G. or N.K.